

## 激光粉末床熔融成形件的翘曲变形监测

陈锦堂, 张凯\*, 刘婷婷\*\*, 邹志永, 李建森, 韦辉亮, 廖文和

南京理工大学机械工程学院, 江苏 南京 210094

**摘要** 在激光粉末床熔融(LPBF)成形过程中,存在由热应力引起的翘曲变形,严重影响零件精度与性能。为了探究熔池辐射光信号与LPBF工艺中的翘曲变形过程的关联关系,为基于熔池辐射光采集的翘曲缺陷监测提供支持,设置了一组实验,成形了翘曲与非翘曲试样,基于统计学方法分析了翘曲与非翘曲试样成形过程中熔池辐射光信号的特性。结果表明,未翘曲变形试样的光强分布较为均匀,无明显梯度,而翘曲变形试样在翘曲区域出现了明显的光强下降。对于翘曲变形的试样,在悬垂层变形尚未发生时,区域光强均值存在较大极差。翘曲试样与非翘曲试样的光强值层间演化趋势不同。随着成形层数的增加,悬垂结构对光强信号的影响逐渐减小,第5层后光强趋于稳定。

**关键词** 激光技术; 激光粉末床熔融; 翘曲变形; 过程监测; 熔池辐射光

**中图分类号** TH16; TP277 **文献标志码** A

**DOI:** 10.3788/CJL231062

## 1 引言

激光粉末床熔融(LPBF)是一种增材制造(AM)工艺,具有成形复杂形状零件、节约材料等优点,近年来结合算法与人工智能技术<sup>[1]</sup>,被广泛应用于航空航天、医疗器械、兵器制造等领域<sup>[2-3]</sup>。然而LPBF工艺易形成较大的热梯度与热应力,导致试样翘曲变形<sup>[4]</sup>,严重影响零件的尺寸精度与力学性能<sup>[5-6]</sup>。

针对LPBF中的翘曲变形问题,国内外许多学者将模拟仿真与实验相结合<sup>[7-8]</sup>,探究翘曲变形机理<sup>[9]</sup>,优化工艺参数与扫描策略模型及支撑结构设计<sup>[10-11]</sup>,研究不同材料的性质<sup>[12]</sup>等。然而模拟仿真方法通常时间成本较大,且不具备实时性<sup>[13]</sup>。通过传感器采集信号结合数据分析,能够在LPBF成形过程中及时监测变形等缺陷的产生,提高成形件质量<sup>[14]</sup>。Bugatti等<sup>[15]</sup>通过在刮刀上安装接触式图像传感器(CIS),在LPBF的铺粉过程中采集数据形成图像,对铺粉状态进行监测。当试样翘曲程度不高时,利用CIS图像并结合简单离焦量测算因子,可以定位出翘曲位置并估算翘曲高度,结果与离线设备测量的形变量高度吻合。Wang等<sup>[16]</sup>通过热电偶及红外相机采集真实零件成形过程中的基板温度与温度场层间演化,分析发现零件温度场与支撑设置密切相关,且变形最大层并不与热梯度最大层完全重合。钦兰云等<sup>[17]</sup>提出了一种激光沉积制造变形检测与开裂预测的新算法,以制件表面的翘曲角及其

变化量作为判断依据,根据翘曲度、翘曲度变化量与制件尺寸的反正切值设定翘曲阈值与开裂阈值,实现了翘曲检测与开裂预测,并通过实验验证了算法的有效性。综上所述,国内外相关研究主要聚焦于通过图像传感器、热传感器等在层尺度监测翘曲变形过程。

光电二极管是LPBF过程监测中常用的传感器,高采样率的特点使其能够在更微观的尺度记录成形过程,还具有鲁棒性好、成本低、可规模化应用的优势<sup>[18]</sup>。此外,熔池辐射光信号与LPBF工艺中的粉层厚度具有关联关系,能反映高度方向的变形,且熔池辐射光强分布与试样温度场也存在关联关系<sup>[19]</sup>。故通过光电二极管采集熔池辐射光信号监测翘曲变形过程具有价值与可行性。为研究熔池辐射光信号与LPBF中翘曲变形过程的关系,并探究通过熔池辐射光信号采集监测LPBF工艺中翘曲变形的的方法,本文设置实验成形了一组悬垂试样,并采集了翘曲及非翘曲试样成形过程中的熔池辐射光信号。结合试样变形量,用统计学方法进行分析,比较了翘曲与非翘曲试样成形过程中的信号特性和层间演化规律。

## 2 实验设置

## 2.1 成形与监测设备

本次实验使用课题组自主研发的LPBF设备,主要由激光器、伺服系统、铺粉装置等组成。其中激光器为连续型红外光纤激光器,额定功率为500 W,激光波

收稿日期: 2023-07-27; 修回日期: 2023-09-04; 录用日期: 2023-11-03; 网络首发日期: 2023-11-17

基金项目: 国家重点研发计划(2022YFB4600800)、国家自然科学基金(52005262)、江苏省前沿引领技术基础研究重大项目(BK20202007)

通信作者: \*zhangkai@njjust.edu.cn; \*\*liutingting@mail.njust.edu.cn

长为 1060 nm,测得的  $1/e^2$  光斑尺寸为 100  $\mu\text{m}$  左右,试样成形在氩气氛围下进行。

图 1 为基于熔池辐射光采集的 LPBF 过程监控系统。在实验过程中上位机控制激光器和振镜,使激光在预设的工艺参数下扫描材料粉末,并记录了对应的光斑坐标。激光作用于材料粉末形成熔池,进而发出

熔池辐射光,熔池辐射光信号经过带通为 830~960 nm 的滤光片后噪声被去除,三个光电二极管传感器接收信号,利用现场可编程板电路对传感器输出的模拟电压信号进行模数转换,并以 100 kHz 的频率发送至下位机。在下位机中,利用自主开发的数据采集软件对数据进行存储、处理和分析。

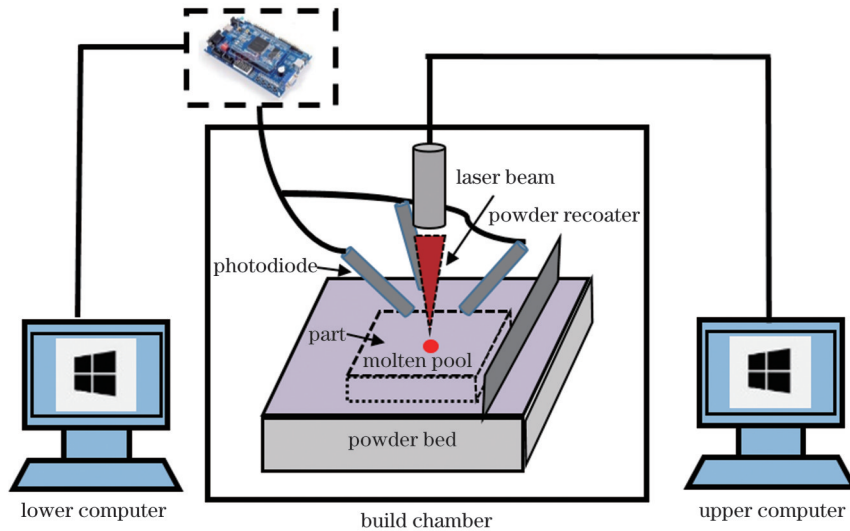


图 1 数据采集设备示意图

Fig. 1 Diagram of data acquisition equipment

## 2.2 实验设计方案

为采集并对比分析翘曲与未翘曲试样成形过程中

的熔池辐射光信号,在实验中成形了 T 字形悬垂结构试样(图 2)。已成形实体和离散金属粉末在未熔化状

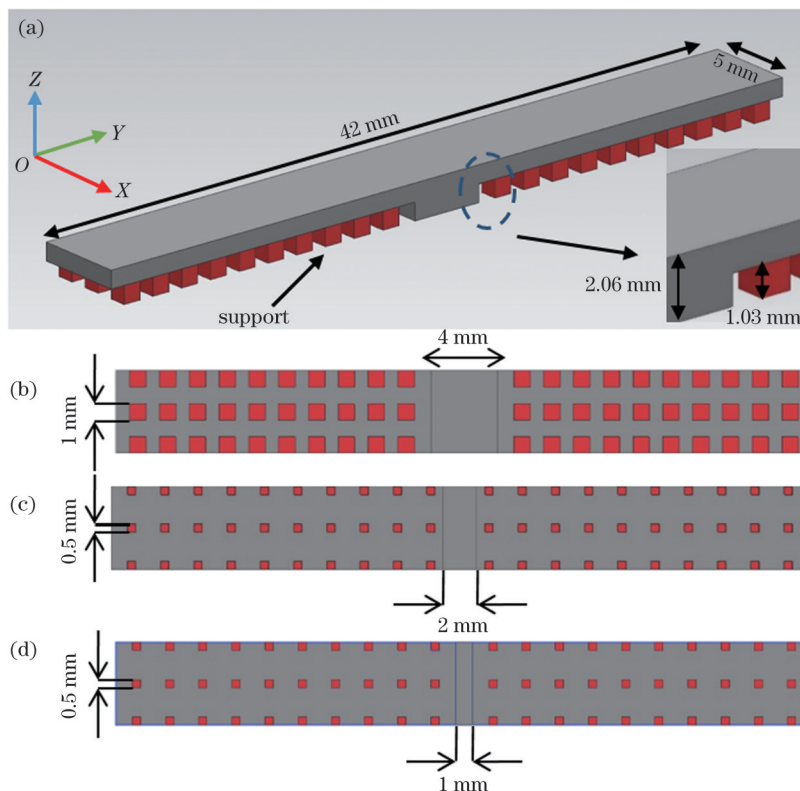


图 2 试样模型及尺寸。(a)试样整体长宽高;(b)试样 1、2 的支撑尺寸;(c)试样 3、4 的支撑尺寸;(d)试样 5 支撑截面尺寸

Fig. 2 Model and sizes of experimental samples. (a) Overall size of sample; (b) size of support cross section of samples 1 and 2; (c) size of support cross section of samples 3 and 4; (d) size of support cross section of sample 5

态下的体积焓和热导率存在较大差异,在温度达到熔点前实体热导率始终高于粉末热导率 10 倍以上<sup>[20]</sup>。在成形悬垂结构的过程中,对于下方为离散粉末的区域,峰值温度较低同时降温较慢,而对于下方为成形支撑的区域,峰值温度较高且降温较快。故悬垂结构更易出现较大的热梯度进而产生热应力,当热应力超过支撑的约束力时就会产生翘曲变形。此外悬垂结构件的翘曲变形量也较易测量。

图 2 为试样外形尺寸与结构。试样与基板的接触面积是影响悬垂试样翘曲变形量的重要因素<sup>[10]</sup>,为了分别得到翘曲与未翘曲试样并采集信号,实验中成形了

三种不同支撑结构及尺寸的 5 个试样。如表 1 所示,为了成形翘曲程度较低或未翘曲试样,试样 1 和 2 设置了较大的与基板接触的面积[图 2(b),试样与基板的接触面积为 80 mm<sup>2</sup>,齿形支撑横截面为边长为 1 mm 的方形],以下称为试样 S80-1 和 S80-2。为了获得具有一定翘曲变形量的样本,试样 3、4 和 5 设置了较小的与基板接触的面积[图 2(c),与基板的接触面积为 25 mm<sup>2</sup>,齿形支撑横截面为边长为 0.5 mm 的方形],以下称为试样 S25-1 及 S25-2。试样 5 的外形尺寸如图 2(d)所示,进一步将试样与基板的接触面积降低至 20 mm<sup>2</sup>,齿形支撑横截面为边长为 0.5 mm 的方形,以下称为试样 S20。

表 1 试样的尺寸  
Table 1 Dimensions of specimen

Sample index	Middle support width /mm	Tooth width /mm	Total contact area between supports /mm <sup>2</sup>
S80-1	4	1	80
S80-2			
S25-1	2	0.5	25
S25-2			
S20	1	0.5	20

由于采用常规工艺参数成形齿形支撑时会出现支撑凸起的现象,降低功率与扫描速度能够改善这一现象<sup>[21]</sup>,故支撑结构与其部分采用不同的工艺参数进行成形。所有试样的主要工艺参数在表 2 中列出。在完成柱状支撑所处层(共 36 层,高度为 1.08 mm,以下称为支撑层)的成形后,进行悬垂结构(共 33 层,高度为 0.99 mm,以下称为悬垂层)成形,同时连续 10 层(即 37~46 层)采集光强信号。

应当指出的是,在完成 37~46 层成形后,试样 S25-1、S25-2 和试样 S20 已发生明显的翘曲变形。为防止损坏实验设备和破坏试样外形,停止了以上试样的成形和信号采集。而试样 S80-1 和 S80-2 未见明显翘曲变形,按计划完成了成形,与翘曲试样保持一致,在 37~46 层进行了信号采集。

表 2 试样的成形参数  
Table 2 Forming parameters of samples

Process parameter	Content	
	1-36 layer	37-69 layer
Laser power /W	195	280
Scanning speed /(mm/s)	1200	1400
Hatch distance / $\mu\text{m}$	105	
Scan strategy	Zig-zag scanning	
Layer thickness / $\mu\text{m}$	30	

2.3 数据处理方法

在试样成形过程中三个光电二极管传感器采集了熔池辐射光强数据,同时上位机记录了激光光斑扫描的

坐标数据。在数据对齐处理后,每个光强数据值都能与一个扫描时的坐标对应,进而能够得到每个采集层的扫描截面光强映射图。为了进一步说明光强数据沿试样长边(Y方向)的变化趋势,对试样扫描截面进行了区域划分,如图 3 所示,沿试样长边每 1 mm 划分为一个区域,并计算得到各个区域的光强均值(例如 area 1 中所有采样点的光强均值为 mean 1)。即针对每个试样采集了悬垂部分 1~10 层的光强数据,每层 42 个区域的光强取均值,每个试样的光强为 420 个区域的光强均值。

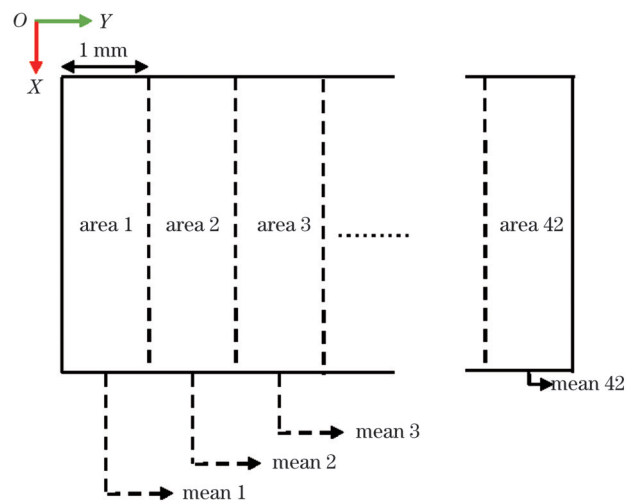


图 3 试样 X-Y 截面区域划分方法  
Fig. 3 Division method of X-Y sections of samples

2.4 变形量测量方法

如图 4 所示,在试样两侧及中心各选取三个测量点,采用三坐标仪分别采集测量点相对基板平面的高



度。具体方法是:计算三个测量点高度的平均值,得出左侧、中间和右侧三个区域相对基板的高度,试样两侧

相对高度分别减去中心相对高度得到高度差( $h$ ),以该值作为衡量试样翘曲变形量的标准。

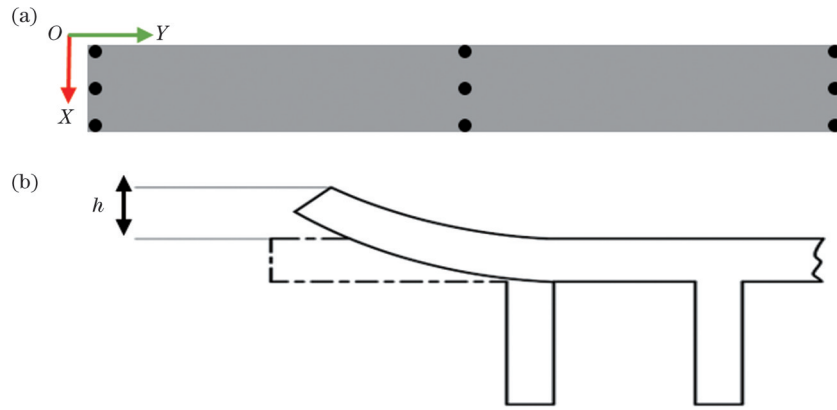


图 4 试样翘曲变形量的测量方法。(a)9个测量点的位置;(b)翘曲变形量定义

Fig. 4 Measurement method of sample warp deformation. (a) Positions of nine measurement points; (b) definition of warp deformation

### 3 结果与分析

#### 3.1 熔池光强信号映射

图 5 所示为试样的实物图及对应试样成形悬垂结构的第 10 层(即第 46 层)时所采集光强信号的坐标映射图。从实物图可以看出:试样 S80-1 及 S80-2 表面平整且有光泽,无明显变形;试样 S25-1、S25-2 及 S20 两侧存在翘曲变形,右侧变形量稍大于左侧。从光强信号的坐标映射图可以看出:试样 S80-1 和 S80-2 对应的光强映射图也较为均匀,无明显的光强梯度分布;而试

样 S25-1、S25-2 及 S20 所对应的光强坐标映射图在翘曲区域出现了明显的光强下降。同时以 S20 为例,在右侧低光强区域有光强短暂升高的狭长区域(图 5 中箭头所指虚线框)。结合实验中观察到的铺粉情况进行分析:当试样翘曲变形达到一定程度时,柔性刮刀沿试样长边刮过后,原本附着于柔性刮刀的粉末被翘曲端留在试样内侧,故在成形过程中产生了较低的熔池辐射光强。同时在对对应映射图的悬垂结构第 10 层(即第 46 层),刮刀由右向左进行铺粉,更多的粉末滞留在试样右端,故翘曲试样右侧的光强低于左侧。

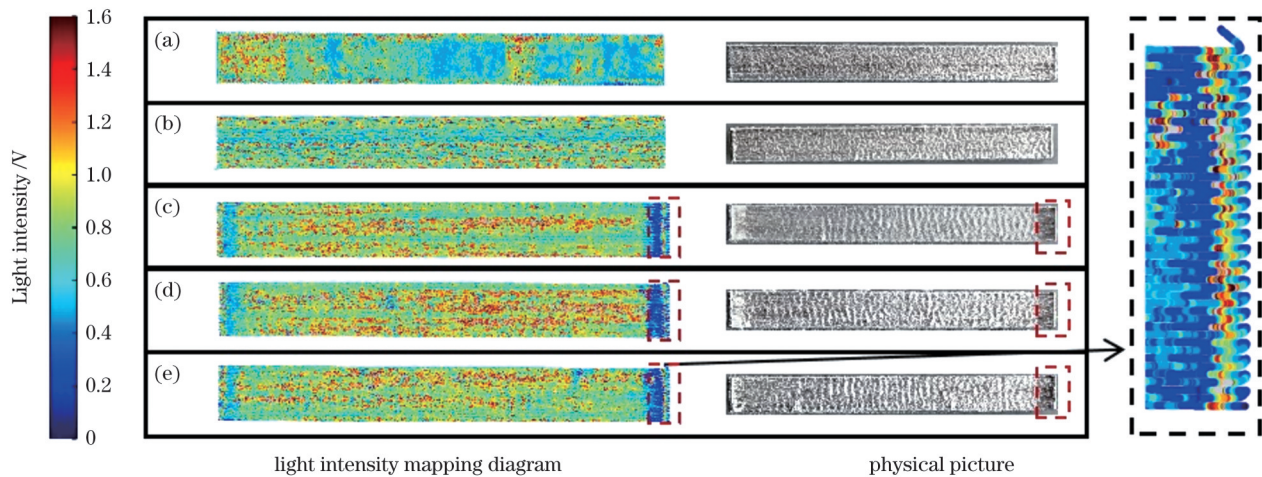


图 5 试样实物图与对应的悬垂末层光强映射图。(a)试样 S80-1;(b)试样 S80-2;(c)试样 S25-1;(d)试样 S25-2;(e)试样 S20

Fig. 5 Physical pictures of samples and corresponding light intensity mapping diagrams of overhanging bottom layer. (a) Sample S80-1; (b) sample S80-2; (c) sample S25-1; (d) sample S25-2; (e) sample S20

#### 3.2 翘曲变形及光强均值

为进一步量化分析试样最终的翘曲变形量,用三坐标仪测量了所有试样的变形量并提取了对应区域的光强均值(详见 2.3 节)。在试样 S80-1 及 S80-2 成形过程中未见明显的翘曲变形,成形时铺粉状态始终正常,而试样 S25-1、S25-2 和 S20 的翘曲变形量较大,最终导致无法继续进行有效铺粉。图 6 为所有试样的翘曲变

形量的测量结果。成形完成后的测量结果显示:试样 S80-1、S80-2 两端与中部的高度差较小,最大差值仅为 0.077 mm;而试样 S25-1、S25-2 和 S20 的两端与中部存在明显的高度差,差值大于 0.789 mm,高出试样 S80-1、S80-2 的 900%;另一方面,试样 S25-1、S25-2 与基板的接触面积为 25 mm<sup>2</sup>,而试样 S20 与基板的接触面积为 20 mm<sup>2</sup>,但翘曲变形量无明显差异。以上结果

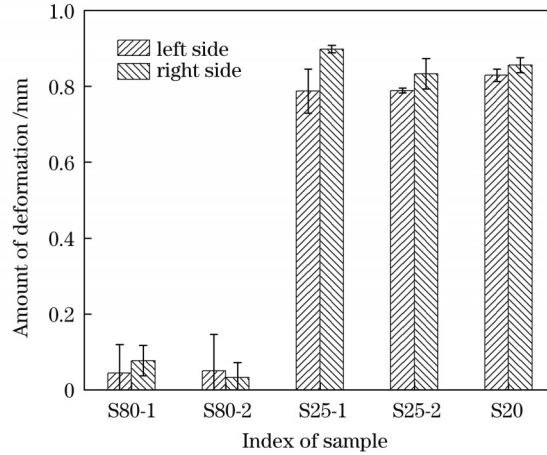


图 6 试样翘曲变形量

Fig. 6 Deformation amounts of samples

表明支撑面积越小,试样越容易发生翘曲变形,但没有明显线性的关联关系。

图 7 为试样末层对应翘曲区域 (Y 为 0~1 mm 及 41~42 mm) 的光强均值。可以看出:未翘曲试样 S80-1 与 S80-2 两端区域的光强均值都较大,最小为 0.93 V;而翘曲试样 S25-1、S25-2 和 S20 两端区域的光强均值都较小,最大为 0.72 V;未翘曲试样两端区

域的光强均值都在一定程度上高于翘曲试样(约高出 30%)。分别观察各个试样的两端光强均值可以发现:对于翘曲变形量较小的一端,对应区域的光强均值普遍较大(试样 S25-2 除外)。这一现象表明,利用熔池光信号能够分辨试样翘曲。结合图 5 可以看出:光强值对变形量有一定敏感性,但两者之间不呈正比例关系。

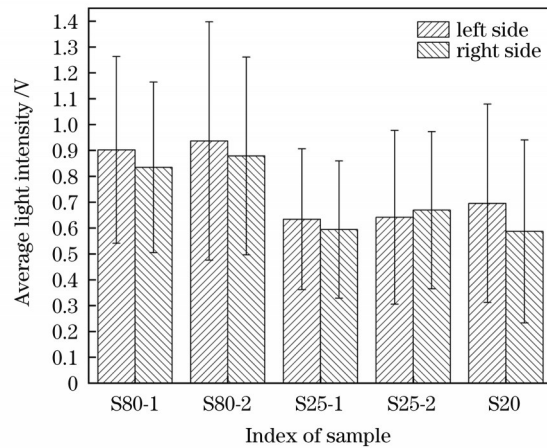


图 7 第 46 层翘曲区域 (Y=0~1 mm, Y=41~42 mm) 对应的光强均值

Fig. 7 Average light intensity corresponding to warping region (Y=0~1 mm and Y=41~42 mm) of layer 46

### 3.3 区域光强与层间演化

为量化分析翘曲变形产生过程与光强值分布的联系,对试样的 X-Y 截面进行了区域划分并计算了各区域光强均值(详见 2.3 节)。图 8 为试样悬垂结构首层即第 37 层沿 Y 方向的光强均值曲线,试样截面图中的箭头方向对应曲线 X 轴正方向。可以看出,在成形翘曲与未翘曲试样时,悬垂结构的首层光强分布存在区别:对于翘曲试样,下层为实体的区域(竖直虚线位置)的光强显著高于其他区域,形成了曲线中的“波峰”;具有相同几何结构的试样在成形时的光强分布具有相似性,非中心区域光强的“振幅”相近。上述现象暗示熔池辐射光强分布与对应位置的峰值温度存在正相关关系<sup>[22]</sup>。该关联关系可以用普朗克黑体发射定

律解释:

$$M(\lambda, T) = \frac{c_1}{\lambda^5} \left( e^{\frac{c_2}{\lambda T}} - 1 \right)^{-1}, \quad (1)$$

式中:  $M(\lambda, T)$  为黑体辐射出射度(单位为  $W/m^2$ );  $\lambda$  为波长(单位为 m);  $T$  为温度(单位为 K);  $c_1$  为普朗克第一辐射常数;  $c_2$  为普朗克第二辐射常数。当计算实际物体的辐射出射度时,还应考虑灰度影响,即在式(1)中增加主要被发射率影响的系数( $\epsilon$ ):

$$M(\lambda, T) = \frac{c_1}{\lambda^5} \epsilon \left( e^{\frac{c_2}{\lambda T}} - 1 \right)^{-1}. \quad (2)$$

由上述定律可知,熔池辐射光强度受波长、发射率与温度的影响,在本研究中滤光片限制了波长带通,而

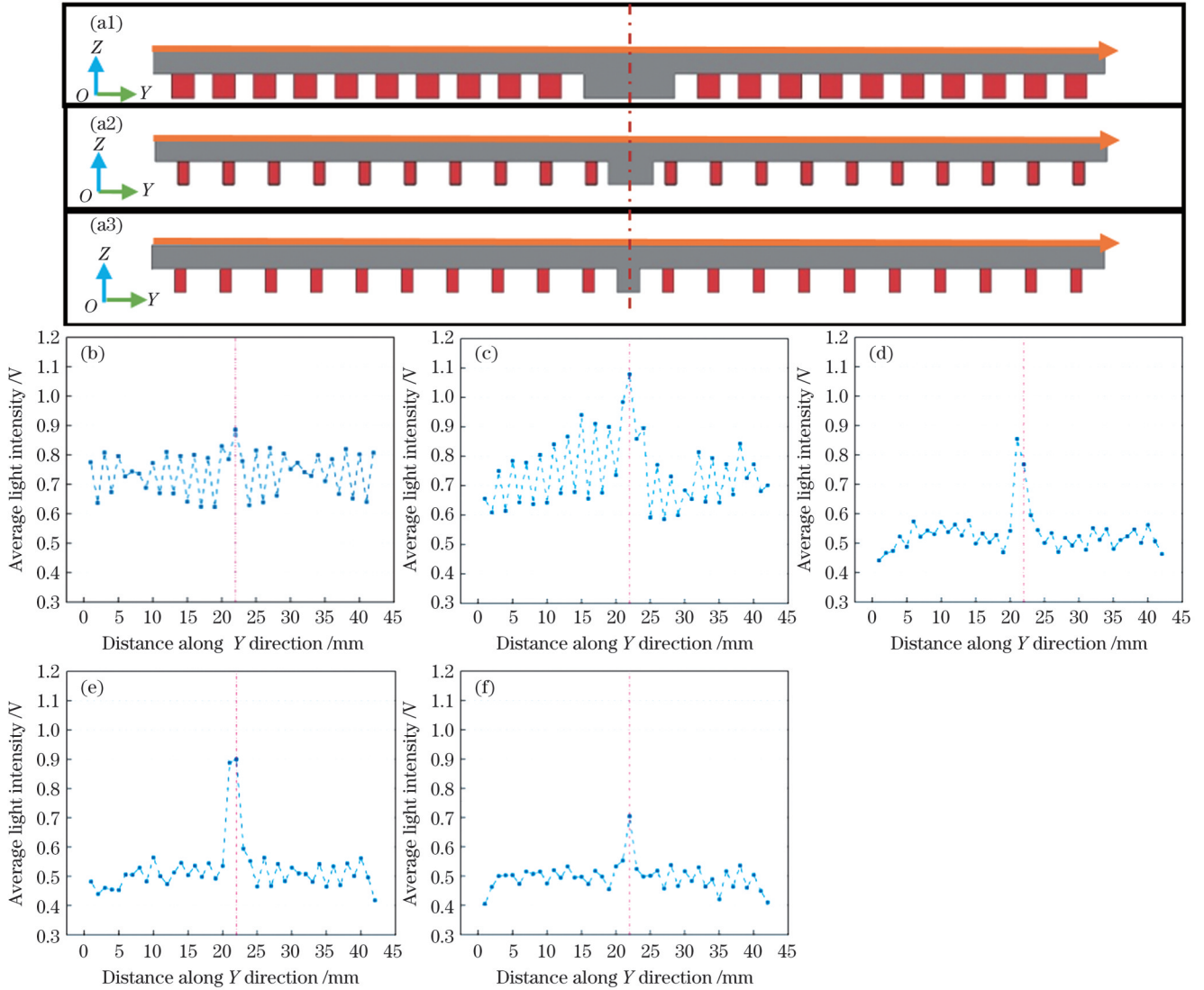


图 8 试样 Z-Y 截面图及试样悬垂首层沿 Y 方向的光强分布曲线。(a1) 试样 S80 的 Z-Y 截面图; (a2) 试样 S25 的 Z-Y 截面图; (a3) 试样 S20 的 Z-Y 截面图; (b) 试样 S80-1 的光强分布曲线; (c) 试样 S80-2 的光强分布曲线; (d) 试样 S25-1 的光强分布曲线; (e) 试样 S25-2 的光强分布曲线; (f) 试样 S20 的光强分布曲线

Fig. 8 Z-Y cross sections of samples and average light intensity distribution curves of overhanging first layers of samples along Y direction. Z-Y cross sections of samples (a1) S80, (a2) S25, and (a3) S20; average light intensity distribution curves of samples (b) S80-1, (c) S80-2, (d) S25-1, (e) S25-2, and (f) S20

发射率主要由材料自身性质决定,故理论上熔池辐射光信号强度与熔池峰值温度存在关联关系。

另一方面,在下方无实体支撑的区域,由于实际层厚的增大,激光作用于粉末的能量密度更小,能量作用的分散形成了不稳定的且峰值温度更低的熔池。LPBF 中的能量密度计算公式为

$$\rho = \frac{p}{vht}, \quad (3)$$

式中:  $\rho$  为能量密度;  $p$  为激光功率;  $v$  为扫描速度;  $h$  为扫描间距;  $t$  为粉末层厚。

综上,该曲线间接反映了试样 Y 方向的温度分布,试样温度场分布相对不均匀,成形过程中热应力较大,故产生了翘曲变形。

为了量化分析成形过程中熔池辐射光强度的层间

演化与翘曲变形的关系,对比了试样  $Y=20\sim 21$  mm 区域(下方为已成形实体,实线箭头处)光强均值和  $Y=41\sim 42$  mm 区域(悬垂区域,虚线箭头处)的光强均值的层间演化(悬垂层 1~10 层, 37~46 层)。如图 9 所示,整体而言,具有相同几何结构的试样的光强层间演变趋势具有相似性,未翘曲试样对应的光强层间波动较大而翘曲试样的光强层间波动较小。在 37~39 层,未翘曲试样 S80-1 和 S80-2 中央区域的辐射光信号强度上升到 1.3 V 以上,而翘曲试样 S25-1 和 S25-2 中央区域的辐射光信号强度呈下降趋势,整体低于 1.0 V,试样 S20 中央区域的辐射光信号强度平稳上升但也不超过 1.0 V。在之后的 7 层中,翘曲试样中央区域的光强始终高于边缘区域的光强,两者均在上升后趋于平稳。而未翘曲试样则不同: 43~46 层边缘区域的光强



超过并始终高于中央区域的光强,二者在 46 层十分接近。

这一现象表明:热应力的形成主要发生在悬垂层的前三层,未翘曲试样各位置的峰值温度变化趋势相

较翘曲试样更为一致,热梯度相对较小。随着成形层数的增加,悬垂结构对光强信号的影响逐渐消除,但热应力仍逐渐积累,最终热应力超过了试样 S25-1 的支撑约束力,导致了翘曲变形,并被光强信号所反映。

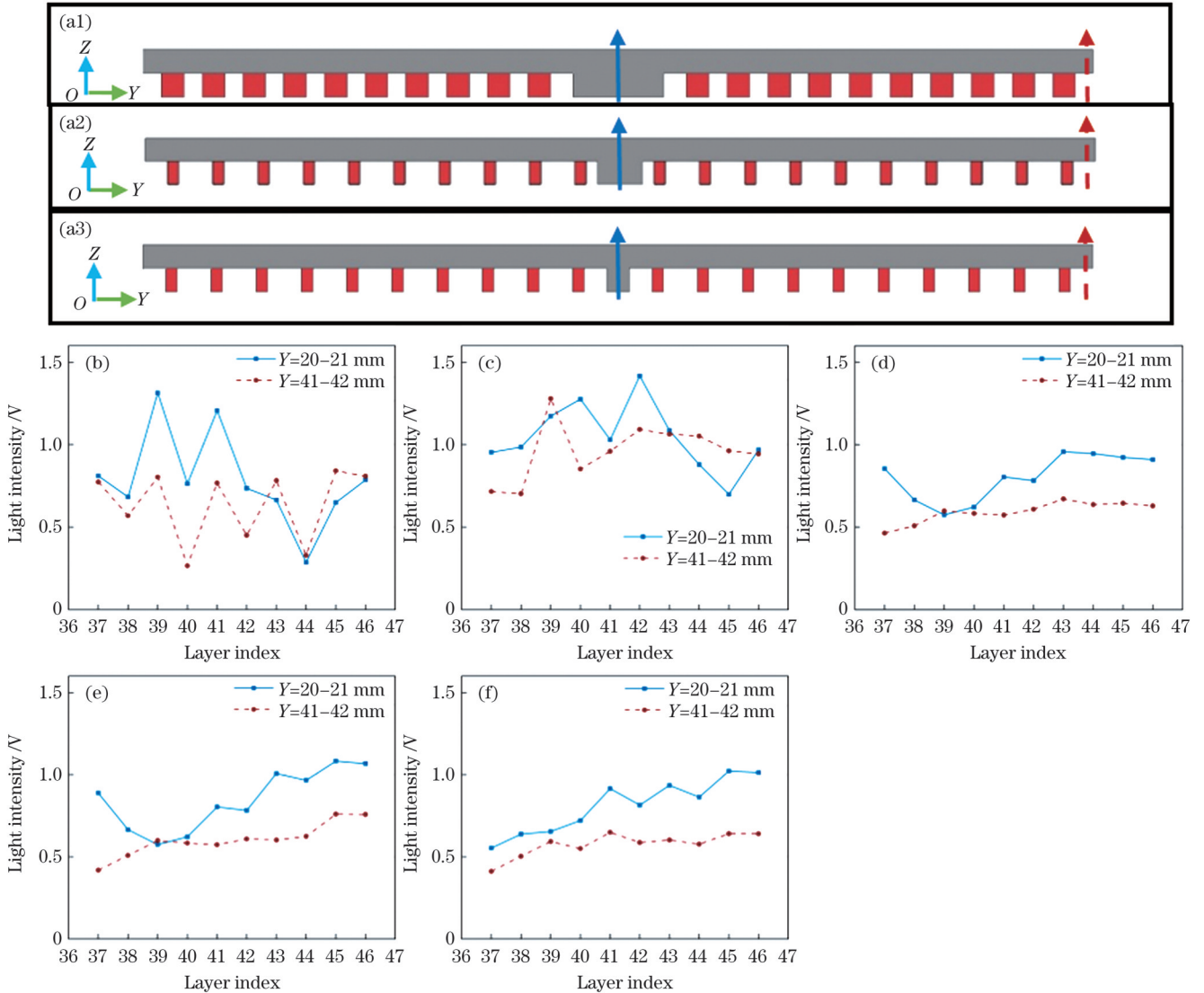


图9 试样 Z-Y 截面图及试样光强的层间演化。试样(a1)S80、(a2)S25、(a3)S20 的 Z-Y 截面;试样(b)S80-1、(c)S80-2、(d)S25-1、(e)S25-2、(f)S20 光强的层间演化

Fig. 9 Z-Y cross sections of samples and interlayer evolution of light intensity in samples. Z-Y cross sections of samples (a1) S80, (a2) S25, and (a3) S20; interlayer evolution of light intensity in samples (b) S80-1, (c) S80-2, (d) S25-1, (e) S25-2, and (f) S20

### 4 结 论

成形了三种不同结构的悬垂试样,采集了熔池辐射光信号。通过试样变形量测量并结合统计学方法,对数据进行了分析,得到以下结论:

1) 翘曲变形试样在翘曲区域出现了明显的光强下降,而未翘曲变形试样的光强分布较为均匀,无明显梯度。

2) 翘曲变形试样在刚开始成形悬垂层且变形尚未发生时,中央实体区域对应的光强“波峰”与该层其他区域光强存在较大的差异。

3) 翘曲试样与未翘曲试样的光强值的层间演化趋势不同。随着成形层数的增加,悬垂结构对光强信号的影响逐渐减小,第 5 层后光强趋于稳定。

4) 试样支撑面积越小,越容易发生翘曲变形,但没有明显的线性关联关系。

### 参 考 文 献

[1] 张宇梁, 钟占荣, 曹洁, 等. “人工智能赋能激光”: 智能化激光制造装备及工艺研究进展[J]. 中国激光, 2023, 50(11): 1101005. Zhang Y L, Zhong Z R, Cao J, et al. Artificial intelligence empowered laser: research progress of intelligent laser manufacturing equipment and technology[J]. Chinese Journal of Lasers, 2023, 50(11): 1101005.

- [2] Rochus P, Plesseria J Y, Van Elsen M, et al. New applications of rapid prototyping and rapid manufacturing (RP/RM) technologies for space instrumentation[J]. *Acta Astronautica*, 2007, 61(1/2/3/4/5/6): 352-359.
- [3] Yap C Y, Chua C K, Dong Z L, et al. Review of selective laser melting: materials and applications[J]. *Applied Physics Reviews*, 2015, 2(4): 041101.
- [4] 吴晓明, 周亚雄, 杨欢庆, 等. 选择性激光烧结翘曲变形抑制工艺[J]. *火箭推进*, 2019, 45(3): 75-80.  
Wu X M, Zhou Y X, Yang H Q, et al. Process study on warp distortion inhibition of selective laser sintering[J]. *Journal of Rocket Propulsion*, 2019, 45(3): 75-80.
- [5] 张国庆, 杨永强, 张自勉, 等. 激光选区熔化成型零件支撑结构优化设计[J]. *中国激光*, 2016, 43(12): 1202002.  
Zhang G Q, Yang Y Q, Zhang Z M, et al. Optimal design of support structures in selective laser melting of parts[J]. *Chinese Journal of Lasers*, 2016, 43(12): 1202002.
- [6] 张凯, 刘婷婷, 张长东, 等. 基于熔池数据分析的激光选区熔化成形件翘曲变形行为研究[J]. *中国激光*, 2015, 42(9): 0903007.  
Zhang K, Liu T T, Zhang C D, et al. Study on deformation behavior in selective laser melting based on the analysis of the melt pool data[J]. *Chinese Journal of Lasers*, 2015, 42(9): 0903007.
- [7] Olleak A, Xi Z M. Efficient LPBF process simulation using finite element modeling with adaptive remeshing for distortions and residual stresses prediction[J]. *Manufacturing Letters*, 2020, 24: 140-144.
- [8] 李湘生, 韩明, 史玉升, 等. SLS成形件的收缩模型和翘曲模型[J]. *中国机械工程*, 2001, 12(8): 887-889.  
Li X S, Han M, Shi Y S, et al. Shrinkage model and warping model of SLS forming parts[J]. *China Mechanical Engineering*, 2001, 12(8): 887-889.
- [9] Yin Q Y, Wei H L, Chen R, et al. Interdependent evolution of deformation, fracture and recovering deposition during laser powder bed fusion[J]. *Additive Manufacturing*, 2023, 72: 103610.
- [10] Khobzi A, Farhang Mehr F, Cockcroft S, et al. The role of block-type support structure design on the thermal field and deformation in components fabricated by Laser Powder Bed Fusion[J]. *Additive Manufacturing*, 2022, 51: 102644.
- [11] 郭朦, 刘凯, 孙婧佳, 等. 扫描策略对激光粉末床熔融 W-Ti 合金致密化、残余应力及力学性能的影响[J]. *中国激光*, 2023, 50(4): 0402003.  
Guo M, Liu K, Sun J J, et al. Effects of laser scan strategies on densification, residual stress, and mechanical properties of W-Ti heavy alloy fabricated by laser powder bed fusion[J]. *Chinese Journal of Lasers*, 2023, 50(4): 0402003.
- [12] Dunbar A J, Denlinger E R, Gouge M F, et al. Comparisons of laser powder bed fusion additive manufacturing builds through experimental *in situ* distortion and temperature measurements[J]. *Additive Manufacturing*, 2017, 15: 57-65.
- [13] Bayat M, Klingaa C G, Mohanty S, et al. Part-scale thermo-mechanical modelling of distortions in laser powder bed fusion-analysis of the sequential flash heating method with experimental validation[J]. *Additive Manufacturing*, 2020, 36: 101508.
- [14] Qin L Y, Wang K, Li X D, et al. Review of the formation mechanisms and control methods of geometrical defects in laser deposition manufacturing[J]. *Chinese Journal of Mechanical Engineering: Additive Manufacturing Frontiers*, 2022, 1(4): 100052.
- [15] Bugatti M, Colosimo B M. The intelligent recoater: a new solution for *in situ* monitoring of geometric and surface defects in powder bed fusion[J]. *Additive Manufacturing Letters*, 2022, 3: 100048.
- [16] Wang Q, Michaleris P, Pantano M, et al. Part-scale thermal evolution and post-process distortion of Inconel-718 builds fabricated by laser powder bed fusion[J]. *Journal of Manufacturing Processes*, 2022, 81: 865-880.
- [17] 钦兰云, 王昆, 王伟, 等. 激光沉积制造翘曲变形检测与开裂预测研究[J]. *中国激光*, 2023, 50(16): 1602105.  
Qin L Y, Wang K, Wang W, et al. Warping detection and cracking prediction of laser deposition manufacturing[J]. *Chinese Journal of Lasers*, 2023, 50(16): 1602105.
- [18] 张婷, 周鑫, 段玉聪, 等. 激光粉末床熔融过程因素与熔池辐射强度关联研究[J]. *中国激光*, 2022, 49(14): 1402206.  
Zhang T, Zhou X, Duan Y C, et al. Relationship between powder bed fusion-laser forming process factors and molten pool radiation intensity[J]. *Chinese Journal of Lasers*, 2022, 49(14): 1402206.
- [19] Demir A G, de Giorgi C, Previtali B. Design and implementation of a multisensor coaxial monitoring system with correction strategies for selective laser melting of a maraging steel[J]. *Journal of Manufacturing Science and Engineering*, 2018, 140(4): 041003.
- [20] Chen C P, Yin J, Zhu H H, et al. Effect of overlap rate and pattern on residual stress in selective laser melting[J]. *International Journal of Machine Tools and Manufacture*, 2019, 145: 103433.
- [21] 林会杰. 激光选区熔化成形悬垂结构过程仿真及工艺研究[D]. 南京: 南京航空航天大学, 2018.  
Lin H J. Simulation and process research of laser selective melting forming suspended structure[D]. Nanjing: Nanjing University of Aeronautics and Astronautics, 2018.
- [22] Mao Z Z, Feng W, Ma H, et al. Continuous online flaws detection with photodiode signal and melt pool temperature based on deep learning in laser powder bed fusion[J]. *Optics & Laser Technology*, 2023, 158: 108877.

## Monitoring of Warping Deformation of Laser Powder Bed Fusion Formed parts

Chen Jintang, Zhang Kai\*, Liu Tingting\*\*, Zou Zhiyong, Li Jiansen, Wei Huiliang, Liao Wenhe  
*School of Mechanical Engineering, Nanjing University of Science and Technology, Nanjing 210094, Jiangsu, China*

### Abstract

**Objective** Laser powder bed fusion (LPBF) is an additive manufacturing (AM) process that has the advantages of forming complex-shaped parts and cutting costs. It is widely used in the aerospace, medical equipment, weapons manufacturing, and other industries. However, in the LPBF process, the material powder is repeatedly heated and melted under the effect of laser energy and then cooled and solidified, which facilitates the formation of a large thermal gradient and thermal stress in the parts, leading to warping



deformation. This type of deformation significantly affects the dimensional accuracy and mechanical properties of parts. By combining sensor signal acquisition with data analysis, deformation defects can be detected during AM to reduce production costs and improve the quality of formed parts. The radiant light signal of the molten pool is sensitive to the thickness of the powder layer during the LPBF process, which may reflect the warping deformation that has already occurred. It is also correlated with the temperature of the molten pool, reflecting the peak temperature at that location, and is related to the temperature field of the sample. Therefore, it has the potential to monitor the thermal stress during warping deformation. To study the relationship between thermal stress-induced warping deformation and the radiant light signal of the molten pool, a method for monitoring warping deformation in the LPBF process by acquiring the radiant light signal of the molten pool is explored in this study. In this study, an overhanging sample is formed during the experiment, and the radiation signal of the molten pool is collected and analyzed. The results show that the radiant light signal can not only monitor warping deformation but also reflect formation process of warping deformation to a certain extent.

**Methods** To collect and compare the radiation light signal of the molten pool during the forming process of the warped and normal samples, T-shaped overhanging structure samples are formed (Fig. 2), and five samples with three different support structures and sizes are designed for the experiment (Table 1). In this process, three sensors collect the radiation intensity signals from the molten pool, and an upper computer records the coordinate data of the laser spots (Fig. 1). After data alignment, each light intensity value corresponds to the coordinates of the laser spot during scanning. To further explain the variation trend of the light intensity signal along the long side (Y-direction) of the sample, the scanning section of the sample is divided into regions, and the average light intensity of each region is calculated. Three measurement points are selected on the sample, and the heights of the measurement points relative to the substrate plane are measured using a coordinate apparatus.

**Results and Discussions** No evident warping deformation is observed in the forming process of samples S80-1 and S80-2, whereas the warping deformations of samples S25-1, S25-2, and S20 are larger (Fig. 6). This result indicates that samples with smaller support areas are prone to warping deformation; however, no noticeable linear correlation is observed. The normal samples S80-1 and S80-2 produce a larger average light intensity at both ends, with a minimum value of 0.93 V, while warped samples S25-1, S25-2 and S20-1 produce lower light intensity at the same area (Fig. 7). This phenomenon indicates that sample warping can be distinguished from the light signal of the molten pool. The light intensity distribution of the first overhanging layer is different between the warped and normal samples. The light intensity of the warped sample in the region where the corresponding lower layer is solid is significantly higher than that in other regions, forming a "wave peak" in the curve (Fig. 8). The above phenomena indicate a correlation between the radiant intensity distribution and peak temperature at the corresponding position and reveal that the evolution trend of the light intensity between the layers of the samples with the same geometric structure. The light intensity of the normal sample fluctuates more between layers, whereas that of the warped sample fluctuates less (Fig. 9).

**Conclusions** In this study, three types of overhanging samples with different structures are formed, and the radiation light signal of the molten pool is collected. Combined with sample deformation measurements and statistical methods, the data are analyzed, and the following conclusions are obtained:

- 1) In the layer after warping deformation, the light intensity of the warped specimen decreases significantly in the warped region, while the distribution of the light intensity of the normal specimen is uniform without a notable gradient.
- 2) For the warped specimen, when the overhanging layer has just been formed, and the deformation has not yet occurred, the light intensity "crest" corresponding to the central solid region of the specimen is quite different from the light intensity in other regions of the layer.
- 3) The interlayer evolution trends of the light-intensity values of the warped and normal samples are different. With an increase in the number of formed layers, the influence of the overhanging structure on the light intensity signal gradually decreases, and the light intensity tends to stabilize after the fifth layer.
- 4) A sample with a smaller support area is more likely to produce warping deformation, but no notable linear correlation exists between these two factors.

**Key words** laser technique; laser powder bed fusion; warping deformation; process monitoring; radiant light from molten pool